PHYSICAL REVIEW A **74**, 052712 (2006)

Classical dynamics of enhanced low-energy electron-ion recombination in storage rings

Maria Hörndl,[1,*] Shuhei Yoshida,[1] Andreas Wolf,[2] Gerald Gwinner,[3] Marek Seliger,[1] and Joachim Burgdörfer[1]
[1]*Institute for Theoretical Physics, Vienna University of Technology, A-1040 Vienna, Austria, EU*
[2]*Max Planck Institute for Nuclear Physics, D-69117 Heidelberg, Germany, EU*
[3]*Department of Physics and Astronomy, University of Manitoba, Winnipeg, MB R3 T 2N2, Canada*

(Received 26 June 2006; published 21 November 2006)

Electron-ion recombination observed in storage ring experiments shows a strong enhancement of the recombination rate for highly charged ions with low-energy electrons relative to what standard radiative recombination rates predict. We present detailed simulations of the toroid and solenoid regions of the electron cooler, analyzing the classical dynamics of an electron in the presence of the Coulomb field of the ion, the homogeneous magnetic field inside the cooler, and the transient electric field in the merging section. Both bound and continuum electron dynamics display partially chaotic motion. For bound states we observe stochastic and quasiperiodic l mixing while for continuum electrons we find transient chaos characterized by a fractal generalized reflection function. We determine the modified radiative and field-induced recombination of the electron with a highly charged ion in a storage ring. The obtained absolute excess recombination rates are compared with the experimental data and, overall, reasonable agreement is found. The scaling of the rate with the average relative energy, the ion charge, the magnetic guiding field, and the electron-beam temperatures is analyzed.

DOI: 10.1103/PhysRevA.74.052712 PACS number(s): 34.80.Lx, 29.20.Dh

I. INTRODUCTION

Electron-ion recombination is a fundamental process of great importance in many areas of basic and applied physics. The cross sections and rate coefficients play an important role for applications in astrophysics [1], plasma physics [2], and accelerator physics. For example, the recombination provides a significant ion loss mechanism during electron cooling of ions in a storage ring. Low-energy electron-ion recombination also supplies a promising route for the production of antihydrogen by recombination of cold positrons with antiprotons [3,4].

While a theoretical understanding and description of radiative recombination (RR) within the framework of quantum electrodynamics (QED) was already provided more than half a century ago, accurate measurements of rate coefficients have been proven difficult due to the smallness of the corresponding cross sections. Only with the recent storage ring and single-pass merged beam experiments, the study of the recombination at low temperatures under well-controlled conditions has become possible [5–14]. In storage ring experiments such as those at TSR, ESR, and CRYRING, the incident ion beam is merged with a cold and magnetically guided beam of electrons in the electron cooler (Fig. 1). The electrons provide not only the cooling medium for the ion beam reducing the rest-frame kinetic energy of the fast ions but also supply a cold target for electron-ion recombination. Remarkably, the experimental rate coefficients observed deviate significantly from the theoretical predictions: the measured recombination rate α shows a strong enhancement beyond the standard radiative recombination rate α_{RR} [15–17] at very low relative energies (typically $\lesssim$1 meV) between electrons and ions. This surprising discrepancy with theory for such an elementary QED process of radiative recombination has led to intensive investigations, both experimentally and theoretically, in the past decade. In a series of measurements at different facilities, recombination rates have been explored for bare ions [5–9,11,12] as well as for complex multielectron ions [5,7,10,11,13,14]. For bare ions the observed enhancement ratio $\alpha/\alpha_{\mathrm{RR}}$ ranges from 1.6 for He^{2+} [6] to a factor of 5 for U^{92+} [9] following a systematic $Z^{2.6}$ dependence [9] where Z is the ion charge. In addition, the dependence of the enhancement on external parameters such as transverse and longitudinal beam temperatures $T_{\perp}$ and $T_{\parallel}$, electron density n_e, and magnetic guiding field B has been determined [7]. Accordingly, the measured excess recombination rate $\Delta\alpha=\alpha-\alpha_{\mathrm{RR}}$ at low relative energy scales as $(kT_{\perp})^{-1/2}$ and $(kT_{\parallel})^{-1/2}$, increases approximately as $B^{0.5}$, and is insensitive to n_e.

Several theoretical models have been proposed to explain the anomalously enhanced electron-ion recombination rates. They range from the influence of three-body recombination [6] and density enhancement due to plasma screening effects [18,19] to enhanced recombination by chaotic dynamics [20,21] and recombination induced by an instantaneous switch-on of the electron-ion interaction [22–24]. None of these models can account satisfactorily and consistently for the observed enhancement.

Point of departure of the present theoretical analysis is that the recombination in a storage ring (Fig. 1) does not take place in free space, i.e., at zero external field, but in the presence of a longitudinal magnetic field ($B\neq 0$) along the cooler axis. Moreover, in the merging section of ion and electron beams near the transition from the toroidal to the solenoidal region a transient motional electric field is present in the ionic rest frame causing inelastic electronic transitions. We note that also in Ref. [22] the enhancement of the RR rate has been attributed to the merging between electrons and ions. However, in that model recombination is caused only by an instantaneous turn-on of the electron-ion *interaction* without considering the electric-field distribution in the tor-

---

[*] Electronic address: maria@concord.itp.tuwien.ac.at

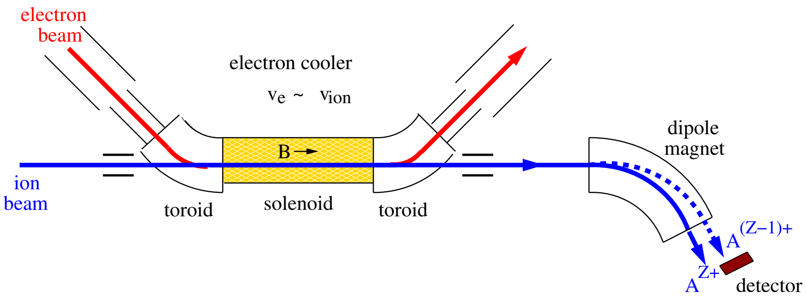

FIG. 1. (Color online) Geometry of the electron-ion interaction in the cooler of a storage ring. In the solenoidal region a constant magnetic field B is present. Toroidal merging and demerging sections feature a spatially varying and thus time-dependent electric field in the ionic rest frame. Recombined ions are separated from the parent ions in the subsequent dipole magnet.

oid, the kinematics of merging, or the properties of the radiative stabilization process [23,24].

In the following we present a detailed analysis of the classical dynamics of individual electron-ion pairs in the electron cooler of the storage ring. Both the curved (toroidally shaped) magnetic-field section, where the electron beam is merged with the ion beam, and the subsequent straight (solenoidal) section where the beams are aligned with each other will be studied. Many-electron effects such as plasma excitations and screening or three-body recombination are neglected from the outset. This appears to be justified in view of the very low ion-electron density ($\sim 10^7$ cm^{-3}). We employ a classical trajectory Monte Carlo (CTMC) method to describe the electronic dynamics in the presence of the projectile ion and external fields. The rationale for employing classical dynamics is twofold: For one, a quantum-mechanical evaluation of the rate coefficients in the presence of the magnetic field constitutes a prohibitively difficult task in view of the two disparate scales involved, the characteristic distances $r \lesssim r^{\mathrm{RR}}$ from which contributions to the RR matrix element originate and the classical cyclotron radius $r_c = v_\perp c/B$ [atomic units (a.u.) are used throughout], which delimits the lateral confinement of the incident electronic wave function in the asymptotic regime. For typical field strengths ($B \approx 42$ mT) and transverse beam energies ($kT_\perp \approx 10$ meV) in the cooler the cyclotron radius amounts to an order of magnitude of $r_c \approx 10^5$ a.u., whereas the distance of the recombined electron is less than

$$r^{\mathrm{RR}} \approx n_R^2/Z, \tag{1}$$

which is of the order of 10–100 a.u. (n_R: maximum principal quantum number of the recombined electron observable in the experiment). An expansion of the electronic wave function using either Coulomb continuum or Landau states as a basis would thus require a huge number of basis states in order to represent the wave function accurately in both the asymptotic region and near the target ion. It is the presence of very large quantum numbers that provides partial justification and a second rationale for invoking classical dynamics. Since the typical cyclotron radius r_c itself is large compared to the magnetic length $l_B = \sqrt{(c/B)} \approx 10^3$ a.u., the electron is, on the average, in Landau states with large Landau quantum numbers $N_L \approx (r_c/l_B)^2 \gg 1$ for which a classical description should be valid.

The classical description has the advantage that the electron dynamics in the external fields can easily be treated nonperturbatively in contrast to a full quantum-mechanical treatment. It is well known that mechanical, i.e., nonradiative capture can be treated within a CTMC approach [25,26]. However, as a one-photon radiative transition is involved in the stabilization of bound states during radiative recombination, quantum transition rates are inevitably involved. Classical dynamics within the present approach serves to determine the distribution of initial states, which then undergo radiative transitions. This initial distribution reflects the fact that the reduced one-body system, a one-electron ion in a magnetic field, features a mixed phase space with partially chaotic dynamics. Electron scattering in the magnetic field develops highly irregular, self-similar structures in the generalized deflection functions ("transient chaos"), whereas the bound-state motion features both quasiperiodic and chaotic dynamics.

The paper is organized as follows. After a brief review of the standard RR theory we analyze the classical dynamics of low-lying continuum and high-lying bound electrons in the simultaneous presence of Coulomb and magnetic fields. We calculate the modified RR rate in the magnetic field as well as the electric-field-induced recombination (FR) rate obtained after radiative stabilization inside the solenoid. The dependence of the total rate coefficient α_{tot} on the average relative energy $\bar{E}$ between electrons and ions will be discussed. The scaling of the corresponding absolute excess recombination rate $\Delta\alpha$ with the magnetic-field strength B, the ion charge Z, and the longitudinal and transverse electron beam temperatures $kT_\parallel$ and $kT_\perp$ is compared with the experimental data. A preliminary account of this work has appeared in Ref. [27].

II. STANDARD RADIATIVE RECOMBINATION THEORY

The standard RR rate α_{RR} is calculated as the convolution of the total cross section $\sigma(E)$ for the RR process with the velocity distribution $f(\vec{v})$ [8–10],

$$\alpha_{\mathrm{RR}} = \langle v\sigma(E)\rangle = \int \sigma(E) v f(\vec{v}) d\vec{v}, \tag{2}$$

where v and E are the relative electron velocity and energy in the rest frame of the ion, respectively, and $f(\vec{v})$ is given by

$$f(\vec{v}) = \frac{1}{2\pi kT_\perp} e^{-v_\perp^2/(2kT_\perp)} \sqrt{\frac{1}{2\pi kT_\parallel}} e^{-(v_\parallel - \bar{v})^2/(2kT_\parallel)} \tag{3}$$

with the temperatures $T_\perp$ and $T_\parallel$ corresponding to the transverse ($v_\perp$) and longitudinal ($v_\parallel$) velocity distributions relative to the direction of the magnetic field and the mean detuning velocity $\bar{v}$ between the merged ion and electron beams defining the average relative energy $\bar{E}=\bar{v}^2/2$.

In the experiment $f(\vec{v})$ is highly anisotropic with $T_\perp \gg T_\parallel$. The total RR cross section is obtained by summing up the contributions from all possible final states up to a maximum contributing principal quantum number n_R determined by field ionization of all higher-lying states in the charge-analyzing dipole magnet downstream from the electron cooler, i.e.,

$$\sigma(E) = \sum_{n=1}^{n_R} \sigma_{\mathrm{RR}}(n,E) = (2.1 \times 10^{-22}\ \mathrm{cm}^2)\sum_{n=1}^{n_R} G_n(E)\frac{Z^4E_0^2}{nE(Z^2E_0+n^2E)}, \quad (4)$$

using the parametrization of Bethe and Salpeter [17]. $E_0 = 13.6$ eV is the Rydberg energy, Z is the charge of the bare ion, and $G_n(E)$ is the Gaunt factor [28] compensating for deviations from the correct quantum result at low n and high values of E. The standard theory does not take into account the magnetic field in the electron cooler. Specifically, the cross section $\sigma_{\mathrm{RR}}(n,E)$ is calculated from dipole transition matrix elements

$$t_{nlm}(\vec{v}) = \langle nlm|d|\psi_c^+(\vec{v})\rangle, \quad (5)$$

between field-free Coulomb continuum states $|\psi_c^+(\vec{v})\rangle$ with an asymptotic velocity $\vec{v}$ and hydrogenic bound states $|nlm\rangle$. While this approximation is well justified for low-lying excited final bound states $|nlm\rangle$ since, typically,

$$\langle r\rangle_n \leqslant r^{\mathrm{RR}} \leqslant 100\ \mathrm{a.u.} \quad (6)$$

[see Eq. (1)] is negligibly small compared to the cyclotron radius r_c,

$$r^{\mathrm{RR}} \ll r_c, \quad (7)$$

it is bound to fail for the initial state that should converge, instead, asymptotically to a product of one-dimensional Coulomb waves along the field direction $\hat{z}$ and Landau states perpendicular to it,

$$\Psi_i^+(\vec{v},\vec{r}) \xrightarrow[r\to\infty]{} \psi_c^+(v_z,z)\varphi_{N_L,m}(\rho,\phi). \quad (8)$$

At small distances [Eq. (6)], on the other hand, Ψ_i^+ should mimic three-dimensional Coulomb waves $\psi_c^+(\vec{v},\vec{r})$. At intermediate distances $r \approx r_c$ neither approximation is appropriate. The scattering wave function becomes fully nonseparable reflecting the transient chaos in the regime when the Coulomb and Lorentz force are of comparable strength. This regime has been previously investigated for the time-reversed process, i.e., photoionization [29,30]. Calculating scattering states in this regime for the present parameter regime is prohibitively complicated [31,32] in view of the large number of coupled channels ($N_L \gtrsim 10^3-10^4$) involved. This observation motivates us to employ classical dynamics of the scattering process in order to determine the effective flux from asymptotic Landau states into the Coulomb region $r \leqslant r^{\mathrm{RR}}$, where the transition to the bound states actually takes place and where Coulomb states are appropriate. It should be noted that the standard expression [Eq. (2)] accounts for magnetic field effects, to some degree, indirectly through the anisotropic distribution of Eq. (3). The magnetic field tends to suppress the coupling of energy between longitudinal and transverse degrees of freedom mediated by the Coulomb interaction. However, the recombination cross section itself pertains to the pure Coulomb problem [Eq. (4)].

We note that for bare ions one-particle recombination, specifically radiative recombination and field-induced capture, is assumed to be dominant, whereas processes involving more than one electron such as dielectronic recombination (DR) and three-body recombination (TBR) can be safely ruled out. DR can only occur for ions carrying electrons into the collision. Contributions from TBR should scale with the electron density as n_e^2. Since n_e is very low ($n_e \approx 10^7\ \mathrm{cm}^{-3}$) in the experiments and the observed recombination rates have been shown to be insensitive to a variation of n_e by a factor of 5 [7], TBR is unlikely to significantly contribute.

III. CLASSICAL DYNAMICS OF ONE-ELECTRON IONS

A. Time evolution in the solenoid

We consider first the effective one-electron problem in the solenoid, i.e., classical dynamics of an electron in the Coulomb field of the ion and the magnetic guiding field $\vec{B}=B\hat{z}$ inside the solenoid of the electron cooler. It is governed in the symmetric gauge by the Hamiltonian

$$H = \frac{p^2}{2} - \frac{Z}{r} + \frac{1}{2c}BL_z + \frac{1}{8c^2}B^2\rho^2, \quad (9)$$

where $\vec{p}=(p_x,p_y,p_z)$ and $\vec{r}=(x,y,z)$ are the relative momentum and coordinate of the electron in the rest frame of the ion, $\rho=\sqrt{x^2+y^2}$ and $L_z=xp_y-yp_x$. The total potential consisting of the Coulomb potential and the diamagnetic potential is not integrable or separable. This gives rise to a mixed phase space with both regular islands and extended regimes of chaotic motion [32]. Since B inside the solenoid is assumed to be homogeneous and thus, in the rest frame of the ion, time independent, the relative energy E is conserved. The transfer of center of mass to relative energy due to the coupling by the field B, neglected in Eq. (9), is exceptionally small and leads to nonconservation of relative energy on the scale of less than 10^{-7} a.u. The classical dynamics generated by the Hamiltonian Eq. (9) is fundamentally different for positive energies ($E>0$) where irregular scattering ensues and for negative energies ($E<0$) where the electron executes either quasiperiodic or chaotic bound motion. The asymptotic initial conditions prior to merging obviously have $E>0$, i.e., they are electron-ion-scattering initial conditions. The electron-ion interaction in the cooler corresponds thus to Coulomb scattering in a moderately strong magnetic field. Note that the quantum threshold for scattering lies at $E_T = \frac{1}{2}\omega_c \approx 10^{-7}$ a.u ($\omega_c=B/c$: cyclotron frequency) rather than $E=0$ because of the minimum energy associated with the lowest Landau level. Negative energies can be accessed by either radiative recombination or nonradiative (i.e., field-

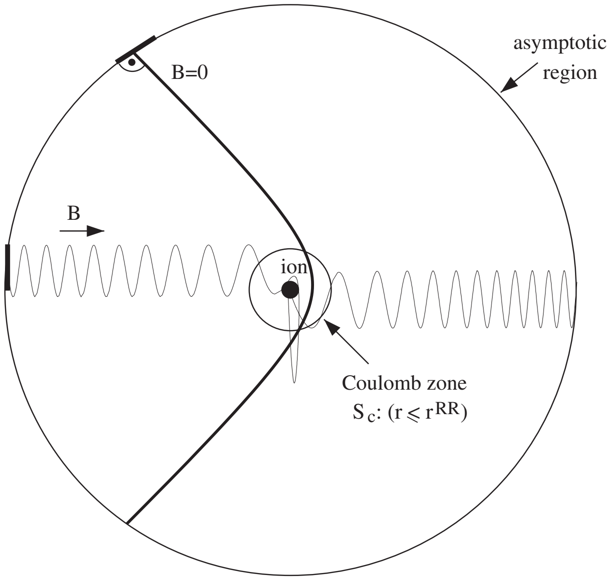

FIG. 2. Electron-ion scattering trajectories in the combined Coulomb and magnetic field ($B \neq 0$) and the pure Coulomb field. Both enter the Coulomb zone S_c within which radiative recombination can occur. Visits are counted by the visit function V_B. For Coulomb hyperbola, $V_C = 1$, while in the presence of a B field, $V_B = i$ ($i > 1$), becomes possible.

induced) recombination due to time-dependent motional electric fields in the merging section.

1. Classical irregular scattering

Two typical scattering trajectories, one in the presence of the magnetic field and one in a pure Coulomb field, are depicted in Fig. 2. They emanate in the asymptotic region where the Coulomb energy is negligible compared to the kinetic energy given by an anisotropic Maxwell-Boltzmann velocity distribution [see Eq. (3)]. In order to determine the flux relevant for RR, we focus on trajectories that reach the Coulomb zone $S_c = \{r | r < r^{\mathrm{RR}}\}$. We characterize this (half) scattering process in terms of a generalized deflection function, in the following referred to as visit function $V(\Gamma)$ where Γ is the subset of initial phase-space coordinates $(\vec{r}, \vec{v})$ resulting in at least one visit of the Coulomb zone. V is integer valued,

$$V(\vec{r}, \vec{v}) = i \quad (i = 1, 2, \ldots), \tag{10}$$

for all $(\vec{r}, \vec{v}) \in \Gamma$. As obvious from Fig. 2, for pure Coulomb trajectories the visit function V_C can take only the value $i = 1$ while in the presence of a magnetic field (V_B) multiple visits ($i > 1$) become possible due to the irregular scattering dynamics. An example of a complex trajectory is shown in Fig. 3 in projections onto different planes in configuration space. The distance function $r(t)$ displays sharp minima signaling a visit of the Coulomb zone S_c.

The visits as a function of the initial coordinates (b, ϕ) in the impact parameter plane oriented perpendicular to the asymptotic velocity vector (for $B = 0$) at fixed initial velocity $(v_\parallel, v_\perp)$ are shown in the phase-space portrait in Fig. 4. It should be noted that the definition of the impact parameter plane is not straightforward in the presence of the magnetic field since in this case two rather than one symmetry breaking axes $(\vec{B}, \vec{v})$ exist. However, by averaging over one period of the helical motion, the average velocity is collinear to $\vec{B}$ and a unique transverse plane can be defined as the average impact parameter plane, i.e., $b = \rho$ and ϕ as the angle between two vectors in the xy-plane, $\vec{b} = (x, y)$ and $\vec{v}_\perp = (v_x, v_y)$. While the Coulomb problem features one singly connected region of initial conditions resulting in single visits, the combined Coulomb and magnetic fields lead to a highly structured phase-space portrait containing self-similar regions of mul-

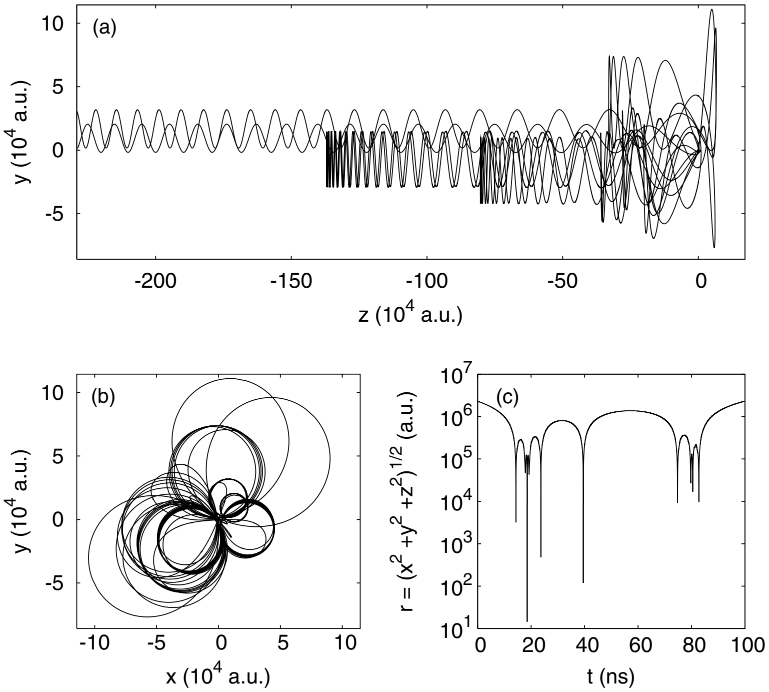

FIG. 3. Electron trajectory in the combined Coulomb [C^{6+} ion fixed at (0,0,0)] and magnetic field ($B = 42$ mT). The projections onto the z-y plane (a), x-y plane (b), and the total distance to the nucleus as a function of the evolved time (c) are shown. Initial velocity $v_\parallel \approx 2.78 \times 10^{-3}$ a.u. parallel to and $v_\perp \approx 1.99 \times 10^{-3}$ a.u. perpendicular to the magnetic field.

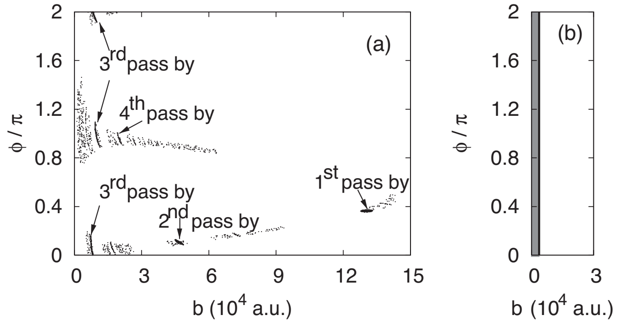

FIG. 4. Phase-space portrait of the visit function $V_B(\vec{r},\vec{v})$ (a) and $V_C(\vec{r},\vec{v})$ (b) at fixed perpendicular and parallel velocities $v_\perp \approx 9.15\times 10^{-3}$ a.u., $v_\parallel \approx 2.74\times 10^{-3}$ a.u., and initial coordinate $z \approx -7.17\times 10^{6}$ a.u. Visits are defined for the Coulomb zone S_c ($r \leqslant r^{\mathrm{RR}} = 100$ a.u.), $B=30$ mT and $Z=6$. b denotes the impact parameter and ϕ the angle between $\vec{b}$ and $\vec{v}_\perp$. Structures in V_B can be assigned to different classes of trajectories as indicated in (a).

tiple visits. The origin of fractal structures in V_B can be understood by investigating individual trajectories. For example, the dense spot at $(b,\phi/\pi)\approx(13\times 10^4, 0.36)$ represents a small connected area of points with nonzero V_B, which corresponds to the initial conditions of trajectories visiting the Coulomb zone when the electron passes by the ion for the first time. Similarly, the spot at $(b,\phi/\pi)\approx(4.7\times 10^4, 0.1)$ is associated with electrons having a visit on their second pass by. The connected regions pertaining to visits on the third and fourth traversals of the ionic plane are likewise visible in Fig. 4(a). The later a visit occurs, i.e., the longer the total propagation time, the higher its sensitivity on the initial conditions becomes. Concurrently, the size of the connected regions to be formed decreases for visits taking place at later times, which is a signature of a hierarchical phase space. As these structures become smaller and smaller, the fractal-like behavior of the visit function in the presence of the B field, $V_B(\vec{r},\vec{v})$, develops. Multiple traversals of the ionic plane increase the probability for recombination and may enhance the radiative recombination rate. The accurate determination of V_B and its integration over initial phase-space coordinates to be performed for scattering calculations is quite difficult requiring high levels of Monte Carlo statistics to reach converged results.

A necessary initial condition for a visit to occur is that L_z is small enough. Near the ion, due to the strong Coulomb interaction, the electron orbit with $E>0$ can be approximated by a Kepler hyperbola whose minimum distance to the ion is given by [33]

$$r_{\min} = \frac{Z}{2E}\left(\sqrt{1+\frac{2EL^2}{Z^2}} - 1\right). \tag{11}$$

Thus, for a given E, L has to be smaller than a certain value $L_{\max}(E)$ in order to generate a visit, i.e., $r_{\min} \in S_c$. In the presence of the magnetic field B, L^2 is not a constant of motion any more and its initial value therefore cannot predict the distance of closest approach during the time evolution. However, due to the cylindrical symmetry of the system [see Eq. (9)] L_z remains conserved in the magnetic field thus providing at least a lower bound for L^2 at closest approach since $L^2 > L_z^2$. Therefore, a necessary (but not sufficient) condition for a visit becomes

$$|L_z| = \left|\frac{B}{2c}\rho^2 - v_\perp \rho \sin\phi\right| < L_{\max}(E). \tag{12}$$

The magnetic-field dependence of V_B reveals this condition clearly. Visits occur only for (b,ϕ) close to $L_z=0$ given by $\phi = \arcsin[B\rho/(2cv_\perp)]$ as depicted by the lines in Fig. 5(a). With decreasing field strength the cyclotron radius increases ($r_c \propto 1/B$) allowing for visits at larger impact parameters b. In turn, the spread of initial angles ϕ with nonzero V_B becomes narrower in order to yield angular momentum projections L_z small enough. For small B the dynamics becomes more Coulomb-like with $V_B(\vec{r},\vec{v})$ becoming less irregular in (b,ϕ) space approaching a singly connected region of phase space. With decreasing B it gets, however, increasingly difficult to determine $V_B(\vec{r},\vec{v})$ with sufficient accuracy due to its sparser representation in the (b,ϕ) space represented in the calculation. Note that in Fig. 5(a) the Coulomb contribution is situated at $\rho \gg 1$ and $\phi \approx \pi(v_\perp > 0)$ since the orientation of the impact parameter plane is different for the cases $B=0$ and $B\neq 0$ (see Fig. 2). Integrals over the visit functions, which enter estimates for recombination, are, however, independent of this orientation. The dependence of the visit function on $v_\perp$ at fixed $v_\parallel$ is illustrated in Fig. 6(a). At large $v_\perp$ the visit function in the magnetic field approaches that of the pure Coulomb field. At intermediate $v_\perp$ the visit function is enhanced, partially due to multiple visits of irregular trajectories. At very small $v_\perp$ the visit function falls below the Coulomb value because in this limit the confinement to helical orbits effectively reduces the available impact parameters for visits. A similar behavior of V_B can be observed as a function of $v_\parallel$ choosing $v_\perp = 0$ [Fig. 6(b)].

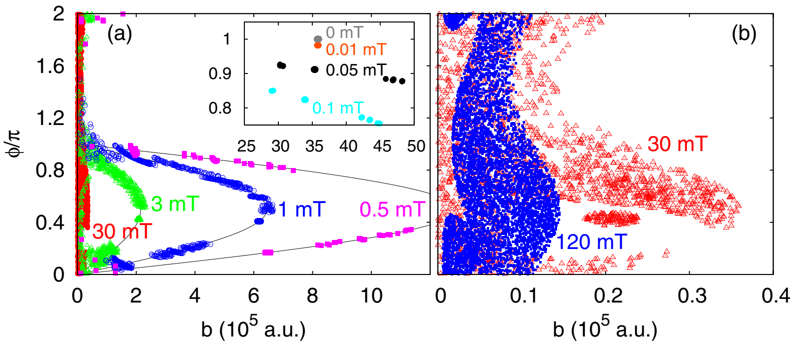

FIG. 5. (Color online) Phase-space portrait of a nonzero visit function $V_B(\vec{r},\vec{v})$ for (a) lower and (b) higher magnetic-field strengths. The initial velocities are fixed to $v_\parallel \approx 2.74\times 10^{-3}$ a.u. and $v_\perp \approx 1.37\times 10^{-3}$ a.u., and the impact plane is located at the coordinate $z\approx -7.17\times 10^{6}$ a.u. Visits are defined for the Coulomb zone S_c ($r \leqslant r^{\mathrm{RR}} = 100$ a.u.). The solid lines in (a) indicate $L_z=0$ corresponding to $\phi = \arcsin[Bb/(2cv_\perp)]$.

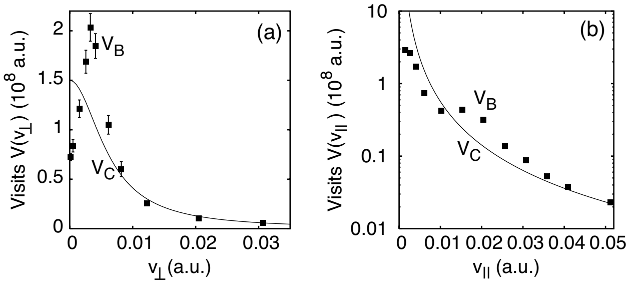

FIG. 6. Visit function $V_B(\vec{v})$ integrated over impact parameters as a function of the initial electron velocity $v_\perp$ ($v_\parallel = 6.14 \times 10^{-3}$ a.u.) (a) and $v_\parallel$ ($v_\perp = 0$) (b) in the combined fields (■) and the pure Coulomb field (line). Visits for the Coulomb zone S_c ($r \leqslant r^{\mathrm{RR}} = 150$ a.u.); $B = 42$ mT and $Z = 6$.

The visit function V_B can now be used to estimate changes in the recombination rate due to magnetic-field induced modification of the flux entering the Coulomb zone relative to that for pure Coulomb scattering, V_C. This allows us to take into account magnetic-field effects in the radiative recombination rate without altering the quantum transition matrix elements [Eq. (5)] themselves as the latter are, to a very good degree of approximation, determined inside the Coulomb zone.

2. Quasiperiodic and chaotic bound motion

For bound motion the presence of a diamagnetic potential manifests itself in the mixing of angular momenta since L^2 is no longer a conserved quantity. Depending on the strength of the Coulomb potential of the parent ion compared to the strength of the magnetic field, electrons are found to move either on chaotic or regular trajectories inside the solenoid (Fig. 7). The relative strength is controlled by the binding energy or principal "quantum" number (principal action) $n = Z/\sqrt{2|E|}$. The latter maintains its significance as an approximate hydrogenic action only for weak B fields and for moderate n. For binding energies close to the ionization threshold and strong magnetic fields the electronic motion is very different from a high n Kepler orbit [Fig. 7(a)]. In this case the cyclotron radius r_c is much smaller than the separation between the electron and the ion. This large separation yields the dynamics separable in the transverse ρ and the longitudinal z direction, i.e., $E = E_\rho + E_z$ where

$$E_\rho = \frac{p_\rho^2}{2} + \frac{L_z^2}{2\rho^2} + \frac{1}{2c}BL_z + \frac{1}{8c^2}B^2\rho^2, \quad E_z = \frac{p_z^2}{2} - \frac{Z}{\sqrt{\rho^2 + z^2}}. \tag{13}$$

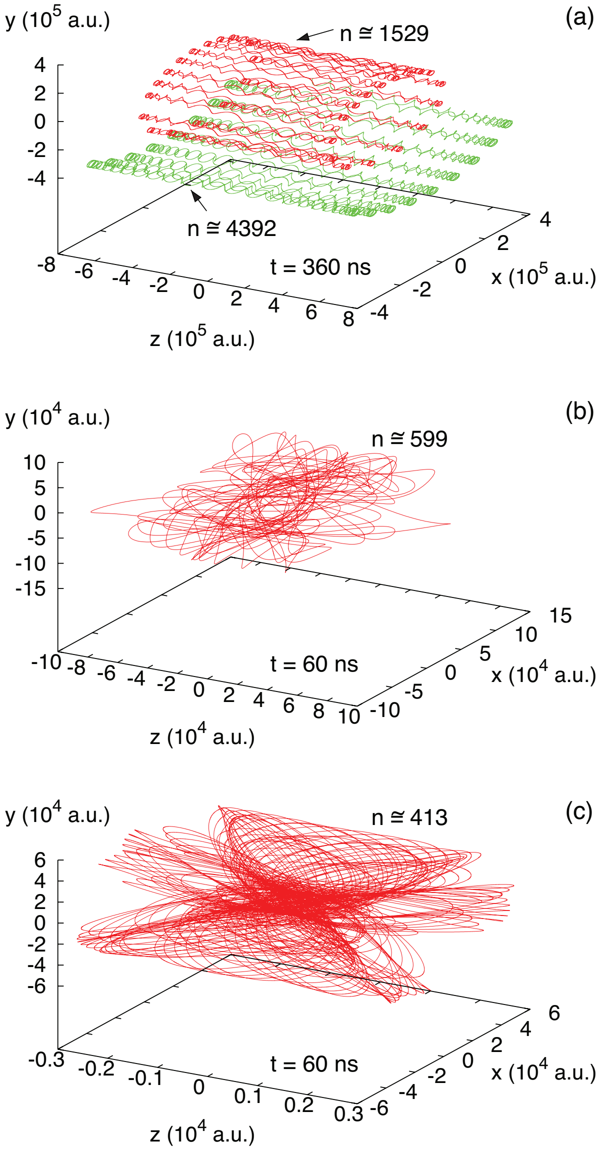

FIG. 7. (Color online) Bound electron trajectories inside the solenoid: (a) guiding center drift motion, (b) chaotic bound-state motion, and (c) perturbed Kepler orbit; $Z = 6$ and $B = 42$ mT corresponding to a cyclotron frequency of $\omega_c \approx 1.8 \times 10^{-7}$ a.u. (a) $E \approx -7.70 \times 10^{-6}$ a.u. ($n \approx 1529$) and $E \approx -9.33 \times 10^{-7}$ a.u. ($n \approx 4392$), respectively. For the $n = 1529$ orbit the transverse electron-ion separation is $\rho \approx 2.5 \times 10^5$ a.u., the electron cyclotron radius $r_c \approx 1.4 \times 10^4$ a.u., the frequency of the oscillations along the field axis $\omega_z \approx 7.0 \times 10^{-9}$ a.u., and the frequency of the $\vec{E} \times \vec{B}$ drift $\omega_D \approx 5.5 \times 10^{-10}$ a.u., whereas for the $n = 4392$ orbit $\rho \approx 4.8 \times 10^5$ a.u., $r_c \approx 1.9 \times 10^4$ a.u., $\omega_z \approx 3.6 \times 10^{-9}$ a.u., and $\omega_D \approx 1.3 \times 10^{-10}$ a.u. (b) $E \approx -5.01 \times 10^{-5}$ a.u. ($n \approx 599$), $\rho \approx 6.6 \times 10^4$ a.u., $r_c \approx 4.6 \times 10^4$ a.u., and $\omega_n \approx 1.7 \times 10^{-7}$ a.u. (c) $E \approx -1.05 \times 10^{-4}$ a.u. ($n \approx 413$), $\rho \approx 7.5 \times 10^3$ a.u., $r_c \approx 2.1 \times 10^5$ a.u., and $\omega_n \approx 5.1 \times 10^{-7}$ a.u. Note that the propagation time is 360 ns in (a) while it is 60 ns in (b) and (c).

In the transverse plane the electron very closely follows the cyclotron orbit. Along the z axis the motion follows the dynamics of an electron in the soft core Coulomb potential with a nearly constant $\rho \simeq \rho_c$ (ρ_c: center of the cyclotron motion, "Guiding center coordinate"). For a bound state ($E_z < 0$) the electron oscillates with a frequency $\omega_z (< \omega_c)$. Due to a small coupling to the motion along the z axis through the Coulomb potential the cyclotron orbit executes a precession of the center of cyclotron motion ($\vec{E} \times \vec{B}$ drift or magnetron motion) around the ion with a frequency $\omega_D (< \omega_z)$. These three motions are clearly visible in Fig. 7(a). The dynamics of these weakly bound and strongly magnetized atoms has been investigated in detail in Refs. [34,35], where the term "guiding center drift atoms" has been introduced. As the rapid cyclotron motion can be averaged over, the dynamics of the electron can be treated by guiding center drift theory. By contrast, if the cyclotron radius becomes comparable to the transverse interparticle separation ($r_c \sim \rho$) and the cyclotron frequency comparable to the Kepler frequency ω_n, i.e., Coulomb and magnetic fields are of competitive strengths, the electron motion becomes chaotic [Fig. 7(b)]. An extension of the corresponding dynamics to the unbound electron ($E>0$) has been seen in Fig. 3. Initially the longitudinal motion is unbound ($E_z>0$). However, every time the electron is scattered by the ion, a strong coupling induces an energy transfer between the longitudinal and the transverse motion. This coupling can reduce E_z to a negative value and the electron can be transiently bound leading to multiple visits to the ion. For larger binding energies the cyclotron radius exceeds the electronic distance to the ion ($r_c > \langle r \rangle_n$) and, similarly, the cyclotron frequency falls below the Kepler frequency ($\omega_c < \omega_n$). The corresponding classical trajectory [Fig. 7(c)] describes now a perturbed Kepler orbit. Finally, for sufficiently deep bound states ($\omega_n \gg \omega_c$) the electronic motion can be well approximated by the unperturbed Kepler motion.

For individual trajectories the angular momentum $l = |\vec{r} \times \vec{v}|$ exhibits quasiperiodic or chaotic fluctuations in the magnetic field (Fig. 8) in contrast to a Kepler orbit in the pure Coulomb field where l is conserved. We note that the angular momentum $\vec{l}$ introduced here is defined via the kinetic momentum $\vec{v}$ while $\vec{L}$ in Eq. (9) exploits the canonical momentum $\vec{p}$. For an evaluation of the RR rate, it is proper to use a gauge-invariant quantity such as $\vec{l}$, whereas for discussing the distance of the closest approach the conserved quantity L_z turns out to be more convenient. For the calculation of radiative recombination, the l distribution of the ensemble generated either during the merging or in the solenoidal section is relevant. Unlike individual trajectories, an ensemble that has initially a statistical l distribution, i.e., $P_{\text{bnd}}(l) \sim (2l+1)/n^2$, remains stationary (Fig. 9). The l distribution of an ensemble of bound electrons does not noticeably change during the propagation through the solenoid but retains the form adopted at the end of the merging process, which is near statistical. Even when the initial distribution is assumed to be nonstatistical, ensemble or time averages over the quasiperiodic or chaotic fluctuations lead to a near-statistical distribution inside the solenoid (Fig. 9). This stationarity and independence of the pathway of formation of bound states simplifies the estimate for the radiative recombination to be discussed below.

B. Classical electron-ion dynamics in the toroidal merging region

In the merging region, the electron beam is guided by a longitudinal magnetic field B along the curvature of the toroid (compare Figs. 1 and 10). The field is parametrized as a function of the opening angle θ with respect to the axis of the solenoid ($\theta \leqslant 0$ in the toroid and $\theta = 0$ in the solenoid) and is given by $B_y = -B \sin \theta$ and $B_z = B \cos \theta$ with y and z defining the toroid bending plane. To ensure guiding of the electrons (beam velocity $\vec{v}_e$ in the laboratory frame), the magnetic field B and the central bending radius R_t of the toroidal field must fulfill the condition $BR_t \gg v_e c$. In addition, a small field component perpendicular to the bending plane, $B_x = v_e c / R_t \ll B$, is required inside the toroid to keep the guiding center motion of the electrons on its bending plane [27,36].

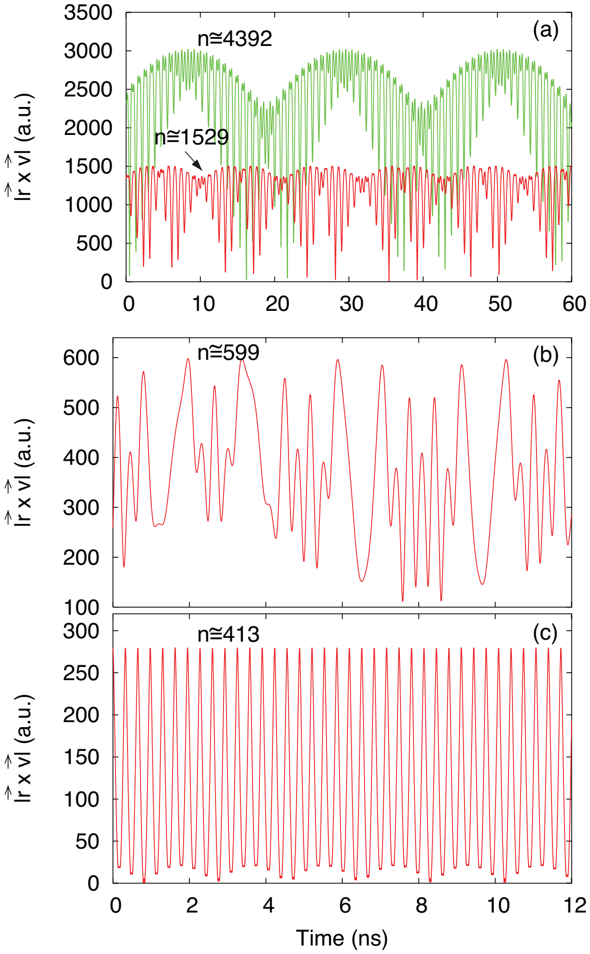

FIG. 8. (Color online) Angular momentum $l = |\vec{r} \times \vec{v}|$ as a function of propagation time through the solenoid for the electron trajectories of Fig. 7. In the presence of a magnetic field ($B = 42$ mT) l is no longer conserved.

In the rest frame of an ion crossing the toroidal region with velocity $\vec{v}_{\text{ion}} = v_{\text{ion}}^z \hat{z}$ these magnetic-field components give rise to motional transverse electric fields $F_x = (v_{\text{ion}}^z / c) B \sin \theta$ (a time varying field as θ varies along the ion orbit) and $F_y = (v_{\text{ion}}^z / c) B_x$ (which drops to zero as the ion leaves the toroid). This electric field tilts the ionic Coulomb potential such as to form a Stark saddle [Fig. 10]. Initially free electrons can pass over the saddle and thus become trapped in the Coulomb potential when the transient electric field is switched off at the entrance of the solenoid. This capture by the Stark saddle was recently observed also in an experiment with a trap-like arrangement [37,38]. This nonradiative, i.e., field-induced mechanical recombination due to time-dependent electric fields opens an alternative pathway to recombination specific to devices such as storage rings that competes with the radiative channel. This process is, in fact, closely interconnected with RR since the mechanical

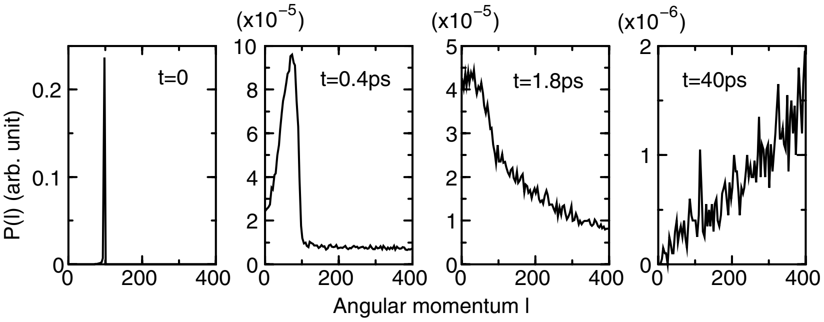

FIG. 9. Approach towards a statistical l distribution starting from a nonstationary distribution due to chaotic fluctuations (n $=599$, $B=42$ mT).

capture is only a necessary but not sufficient condition for recombination. In a second step, radiative decay of the transiently formed Rydberg states to lower levels inside the solenoid stabilizes a fraction of these weakly bound electrons thereby preventing field ionization in the toroidal demerging section (see Fig. 10) [39]. Only sufficiently deep bound electrons with principal quantum numbers $n \leqslant n_R$ contribute to the experimentally observed effective recombination rate. These radiative bound-bound transitions closely mirror free-bound transitions leading to similar parameter dependences as the RR channel. In the following we simulate electric-field-induced recombination (FR) in the merging region and radiative stabilization inside the solenoid using the parameters of the TSR electron cooler, where the toroid has a bending radius of $R_t=80$ cm and an opening angle of $\theta=-45$ degrees.

The electron-ion dynamics during merging is described in the symmetric gauge by the Hamiltonian

$$H=\frac{1}{2}\left(\vec{p}+\frac{1}{2c}[\vec{B}(\vec{r},t)\times\vec{r}]\right)^2-\frac{Z}{r}+\vec{r}\cdot\vec{F}(\vec{r},t) \qquad (14)$$

with the classical electron momentum $\vec{p}$ and coordinate $\vec{r}$ in the rest frame of the ion and the electric- and magnetic-field strengths as discussed above (see Ref. [36] for details). The time-dependent electric field $\vec{F}$ allows for energy gain and loss of the electron during the merging process. The relative energy of the electron-ion system $E=v^2/2-Z/r$ determines whether a bound state with $E<0$ is formed during the merging process. Therefore, the distribution of E at the end of the toroid determines the efficiency of the first stage of nonradiative recombination. Moreover, the distribution among angular momentum states controls the efficiency of subsequent radiative stabilization in the solenoid. Note that at the end of the toroid, the Hamiltonian [Eq. (14)] reduces to that inside the solenoid [Eq. (9)]. We start the propagation of the electron at a distance of 5.6 cm ($\theta\approx-4$ degrees) prior to the solenoid, where the spatial overlap of the electron and ion beams becomes effective. The initial ensemble of electrons is distributed spatially uniformly within a sphere with radius $R_{\text{ini}}=(1/2)n_{\text{ion}}^{-1/3}$ (n_{ion}: ion density) in coordinate space and Maxwell-Boltzmann distributed according to Eq. (3). For beam velocities in the laboratory, $v_{\text{ion}}/c=0.09$, and typical magnetic guiding fields at the TSR (20 mT$\leqslant B \leqslant$70 mT [7]) the strength of the dipole field amounts to $B_x\approx 0.2$ mT to achieve a properly merged electron beam. Accordingly, the center of the initial electron distribution moves such that at the end of the toroid the electron at the center merges with the ion.

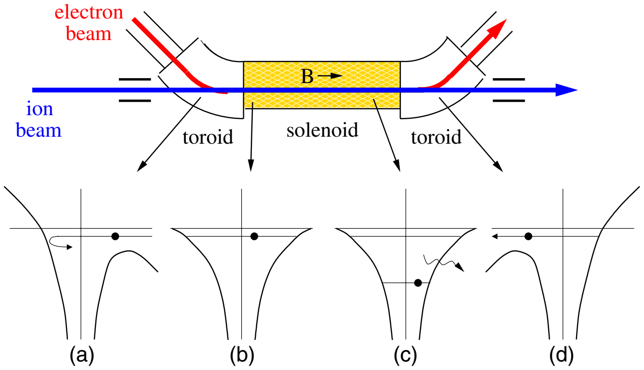

FIG. 10. (Color online) In the toroidal region motion-induced transverse electric-field components in the rest frame of the ion give rise to a time-dependent saddle-point potential. Initially free electrons can pass over the saddle (a) and get trapped inside it (b) when the transient field disappears as the ion enters the solenoid. Radiative decay of the formed Rydberg states inside the solenoid (c) could prevent a small fraction of the electrons from being field-ionized again at the toroidal demerging section (d).

Figure 11 illustrates the evolution of E during the merging process. The broad initial energy distribution [see the inset in Fig. 11(a)] continuously narrows during the merging and shifts to lower values of E. During the gradual approach of the electrons towards the ions in momentum space $\vec{v}_e$ increasingly matches $\vec{v}_{\text{ion}}$ as θ tends to zero. Bound states are formed only during approximately the last 100 ps of the merging process (see the inset in Fig. 11(b) and Table I). For typical storage ring conditions the vast majority of electrons end up in $E>0$ states at the end of the toroid. Only a small fraction of the electrons form (transiently) bound states after the merging is complete. In the case of our CTMC data in Table I, the total bound-state fraction is approximately two percent. Therefore, large ensemble sizes ($\gtrsim 10^8$ trajectories) are required to determine the bound-state (nl) distribution $P_{\text{bnd}}(n,l)$ after the merging and, subsequently, the radiative stabilization inside the solenoid. We have investigated the n-resolved bound-state fractions $P_{\text{bnd}}(n)=\Sigma_l P_{\text{bnd}}(n,l)$ for different ion charges Z and magnetic guiding fields B at the end of the toroid (Fig. 12). While the dynamics is calculated with the magnetic field present, the mapping of the electron energies onto the classical n distribution is performed using the pure Coulombic expression $n=Z/\sqrt{2|E|}$.

The majority of the captured electrons end up in very large principal quantum numbers ($n\gtrsim 1000$) at the end of the

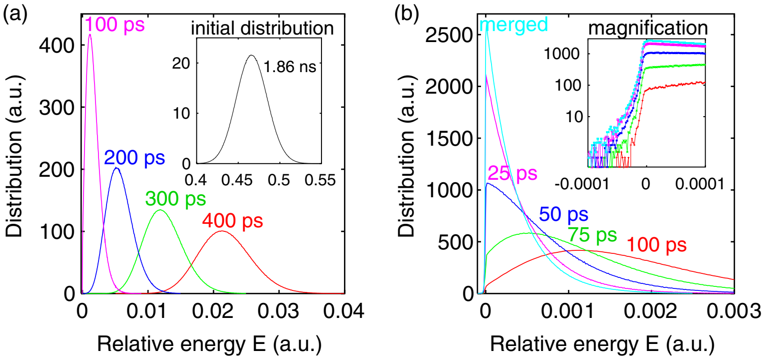

FIG. 11. (Color online) Relative energy distributions during the merging of C^{6+} ions with electrons at the TSR electron cooler with $B=42$ mT and $B_x \approx 0.2$ mT ($kT_\perp = 10$ meV, $kT_\parallel = 0.06$ meV, $\bar{E} = 0.03$ meV, and $R_{\mathrm{ini}} = 8.825 \times 10^5$ a.u.) for different times prior to the completion of the merging process, i.e., $t=0$ at the end of the toroid with $\theta=0$. The inset in (a) shows the initial distribution and the inset in (b) displays a magnification of the distributions around $E=0$.

toroid. The n distribution falls off precipitously towards lower values of n. Even with our large ensemble sizes (3.5×10^8 trajectories) there is typically less than one event for $n \lesssim 100$. The determination of $P_{\mathrm{bnd}}(n)$ at such small n has therefore been performed by a smooth extrapolation from higher n values with a continuous slope (indicated by the lines in Fig. 12). The peak position $n_{\mathrm{peak}} = \sqrt{R_{\mathrm{ini}} Z}$ is related to the spatial extent of the initial ensemble (sphere with radius R_{ini}). Note that in the presence of small electric stray fields inside the solenoid (few V/cm), the bound electrons will be field ionized when $n > n_F$ where n_F is the maximum quantum number to survive stray field ionization. In general, $n_F < n_{\mathrm{peak}}$. Whereas an increase in Z considerably enhances the cumulative bound-state fraction due to the increased Coulomb potential, an increase of B and thus of the transient electric field F during the merging displays a more subtle effect on the population of Rydberg states: increasing the relative probability of low-lying bound states while leaving the total bound-state probability essentially unchanged.

The classical angular momentum l is extracted from our CTMC calculations via $l = |\vec{r} \times \vec{v}|$ with the magnetic field present. The calculated angular momentum distribution $P_{\mathrm{bnd}}(n,l)$ (with n fixed) of field-induced captured electrons after the merging, closely follows the statistical weight $\sim 2l+1$ up to high values of l, corresponding to the m degeneracy for a fixed value of n [27]

$$P_{\mathrm{bnd}}(n,l) = P_{\mathrm{bnd}}(n) \frac{2l+1}{n^2}. \tag{15}$$

The statistical distribution of l (up to $l \leq n_{\mathrm{peak}}$) after merging (Fig. 13) in the toroid agrees well with the prediction for the dynamics in the solenoid (Fig. 9), in particular the initial statistical distribution remains stationary inside the solenoid. Note that the deviation from the statistical distribution at very high l ($\gtrsim 1000$) is a consequence of the cutoff n_{peak} in the n distribution (Fig. 12) and without observable consequences for the calculated recombination rates.

IV. CALCULATION OF EFFECTIVE RECOMBINATION RATES

The classical phase-space distributions of both unbound ($E>0$) and bound ($E<0$) electron-ion pairs, determined in the previous section, influence the effective recombination rate and need to be considered when the standard value α_{RR} is compared with that measured in storage ring experiments. The classical phase-space distribution serves now as input to calculate the effective one-particle recombination rate including both direct radiative recombination in the presence of a magnetic field and nonradiative field-induced recombination followed by radiative deexcitation. The total recombination rate in the electron cooler is given by

$$\alpha_{\mathrm{tot}} = \alpha_{\mathrm{RR}}^{B} + \alpha_{\mathrm{FR}}, \tag{16}$$

where α_{RR}^{B} is the radiative recombination rate modified by magnetic-field effects and α_{FR} is the effective recombination rate by field-induced capture followed by radiative stabilization. We also define an excess recombination rate as

$$\Delta\alpha = \alpha_{\mathrm{tot}} - \alpha_{\mathrm{RR}}. \tag{17}$$

The strategy of modifying the radiative recombination rate in the presence of a magnetic field is to leave the transition matrix element for RR pertaining to the Coulomb zone unchanged [see Eqs. (4) and (5)] while the effective flux of electrons from the asymptotic Landau region into the Coulomb zone is modified. Accordingly, the RR rate under the influence of a magnetic field B, α_{RR}^{B} can be calculated taking into account the visit function V_B as

$$\alpha_{\mathrm{RR}}^{B} = \int \sigma(E) v \frac{\int d^2 b V_B(\vec{r},\vec{v})}{\int d^2 b V_C(\vec{r},\vec{v})} f(\vec{v}) d\vec{v}, \tag{18}$$

where $V_C(\vec{r},\vec{v})$ is the visit function in the pure Coulomb case. The anisotropic Maxwell-Boltzmann distribution in the

TABLE I. Fractions of bound states accumulated during the merging for the distributions illustrated in Fig. 11.

Time prior to the end of the toroid (ps)	200	100	75	50	25	0
Fraction of bound states P_{bnd}	≈ 0	0.00055	0.00279	0.00833	0.01682	0.02119

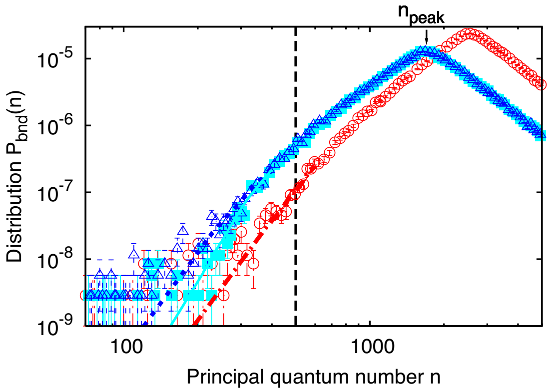

FIG. 12. (Color online) Principal quantum number $n=Z/\sqrt{2|E|}$ distributions after the merging between electron and ion beams with $kT_\perp=10$ meV, $kT_\parallel=0.06$ meV, $\bar{E}=0.03$ meV, and $R_{\text{ini}}=8.825\times10^5$ a.u.; △ and dotted line (blue): $B=42$ mT, $Z=6$; ○ and dashed-dotted line (red): $B=42$ mT, $Z=14$; ■ and full line (light blue:) $B=10$ mT, $Z=6$. All distributions are normalized and obtained with 3.5×10^8 trajectories. The cutoff for stray fields at $n_F\simeq500$ (corresponding to ~2 V/cm) (dashed line) and the peak position $n_{\text{peak}}=\sqrt{ZR_{\text{ini}}}$ are indicated.

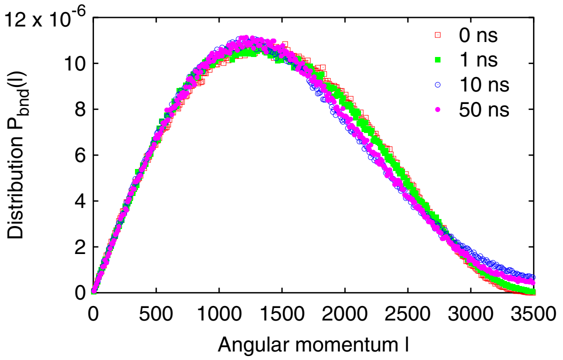

FIG. 13. (Color online) Angular momentum distribution of the bound-state electrons generated during the merging with C^{6+} ions at the TSR ($B=42$ mT, $kT_\perp=10$ meV, $kT_\parallel=0.06$ meV, $\bar{E}=0.03$ meV, and $R_{\text{ini}}=8.825\times10^5$ a.u.) after different propagation times through the solenoid. $t=0$ refers to the entrance into the solenoid.

cooler is denoted by $f(\vec{v}_\perp,v_\parallel)$. Note that $(\vec{v}_\perp,v_\parallel)$ is defined relative to $\vec{B}$ rather than relative to $\vec{b}$. The integral over the impact plane $\int d^2b$ is taken at a distance to the ion where the Coulomb energy is negligible in comparison to the kinetic energy $(v_\parallel^2+v_\perp^2)/2$. At such large distances, the anisotropic Maxwell-Boltzmann velocity distribution $f(\vec{v})$ is essentially unperturbed.

The calculation of α_{FR} proceeds in two steps: First, the field-induced capture probability $P_{\text{bnd}}(n,l)$ due to time-dependent motional electric fields during the merging process is determined (see Sec. III B). The effective recombination probability is estimated from the subsequent radiative relaxation in the solenoid region until the projectile reaches the demerging magnet at time τ_f ($\tau_f=60$ ns in the TSR experiment [7]) as

$$P_{\text{FR}}(\tau_f)=\sum_{n,l}N_{\text{bnd}}(n,l)[1-e^{-\tau_f/\tau(n,l)}]\tau(n,l)W(n,l), \quad (19)$$

where $N_{\text{bnd}}(n,l)=(4/3)\pi R_{\text{ini}}^3 n_e P_{\text{bnd}}(n,l)$ is the average number of electrons found in the state n, l at the end of the merging process and $\tau(n,l)$ is the radiative mean lifetime of the given Rydberg state [40]. The factor $[1-e^{-\tau_f/\tau(n,l)}]$ is the integrated radiative decay probability and $\tau(n,l)W(n,l)=\sum_{n'\leqslant n_R,l'}\tau(n,l)W(n,l\rightarrow n',l')$ describes the branching into all states with $n'\leqslant n_R$. The radiative decay rate from state (n,l) to (n',l') per unit time is given by [17]

$$W(n,l\rightarrow n',l'=l\pm1)=\frac{4}{3}\frac{\omega^3}{c^3}\frac{\max(l,l')}{2l+1}(R_{nl}^{n'l\pm1})^2. \quad (20)$$

In Eq. (20) ω denotes the energy of the emitted photon. The integral over the radial wave functions $R_{nl}^{n'l\pm1}=\int_0^\infty R_{nl}R_{n'l\pm1}r^3dr$ can be evaluated in closed form. In line with the discussion above, we assume that the field-free ($B=0$) rates can be used. This approximation may be justified for averages over a large number of contributing l,l' states due to the invariance of $P_{\text{bnd}}(n,l)$ inside the solenoid [41] but needs to be tested in particular when the contributions from nearly circular states are expected [42,43]. $W(n,l)$ scales as n^{-3} (deviations from this scaling can only be observed at small n for the largest values of l) and strongly decreases with increasing l. Correspondingly, radiative stabilization is strongly favored for initial states with lower n and l quantum numbers. We note that for high n the evaluation of the hypergeometric functions ${}_2F_1$ involved in the calculation of $R_{nl}^{n'l'}$ [17] eventually becomes unstable. We thus employ the extrapolation $R_{nl}^{n'l'}\propto n^{-3/2}$ into the high n region.

Since $\tau_f\ll\tau(n,l)$ for all relevant (n,l), Eq. (19) can be simplified to

$$P_{\text{FR}}\approx\tau_f\sum_{n,l}\sum_{n',l'}N_{\text{bnd}}(n,l)W(n,l\rightarrow n',l') \quad (21)$$

using the statistical population of l, $N_{\text{bnd}}(n,l)=(2l+1)N_{\text{bnd}}(n)/n^2$. The probability for radiative stabilization of transient bound states per ion and per revolution in the ring finally reads

$$P_{\text{FR}}=\tau_f\sum_{n>n_R}N_{\text{bnd}}(n)\sum_{n'=1}^{n_R}W(n\rightarrow n')$$
$$=\tau_f\sum_{n>n_R}N_{\text{bnd}}(n)\sum_{n'=1}^{n_R}\frac{4\omega^3}{3c^3}\frac{1}{n^2}\sum_{l'=0}^{n'-1}\sum_{l=l'\pm1}\max(l,l')(R_{nl}^{n'l'})^2. \quad (22)$$

Note that the evaluation of P_{FR} only requires $N_{\text{bnd}}(n)$ (see Fig. 12) from the simulation. The transition rate $W(n\rightarrow n')$ after summation over l and l' scales as n^{-5}.

The linear approximation in τ_f used to derive Eq. (21) faces the conceptual difficulty that the feeding mechanism of the radiative decay channel given by the formation of bound states during the merging is transient and stops after the merging is completed. Thus, inside the solenoid the source

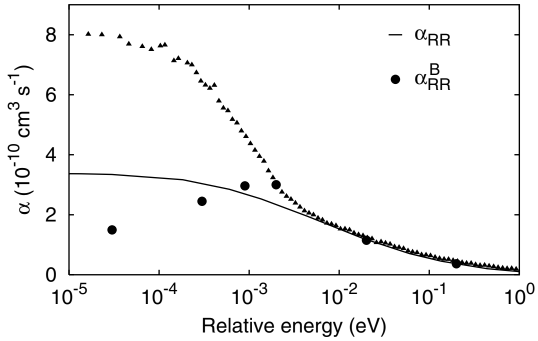

FIG. 14. Recombination rate for C^{6+} ions at $B=42$ mT as a function of the relative energy between electrons and ions. The standard RR theory α_{RR} [Eq. (2)] (line), the experimental data [7] (▲), and α_{RR}^{B} (●) [Eq. (18)] are shown. $kT_{\parallel}=0.2$ meV, $kT_{\perp}=10$ meV, and $n_R=30$.

term for radiative stabilization gets continuously depleted, conflicting with the concept of a constant rate coefficient. However, for long-lived high-lying states $\tau(n,l) \gg \tau_f$ this depletion, i.e., the decrease of available Rydberg states due to preceding radiative decay processes, can be safely neglected and, in analogy to RR, a rate coefficient α_{FR} can be defined for the radiative stabilization channel as

$$\alpha_{\mathrm{FR}} = \frac{P_{\mathrm{FR}}}{n_e \tau_f}. \tag{23}$$

This recombination rate has the remarkable property that it converges towards the standard RR rate in the limit of positive initial electron energies. Equations (22) and (23) will be evaluated in the following for the parameters of Ref. [7], $n_e=7.0\times10^6$ cm^{-3} and $R_{\mathrm{ini}}=8.825\times10^5$ a.u. (corresponding to $n_{\mathrm{ion}}=1.23\times10^6$ cm^{-3}).

Due to the rapid decrease of $W(n\rightarrow n')$ the vast majority of the bound states formed will be reionized again in the toroidal demerging section where the Coulomb barrier gets depressed a second time (see Fig. 10). Only a miniscule fraction will have radiatively decayed to a state n' sufficiently deeply bound to escape the demerging toroid without field ionization. In particular, high-lying initial states ($n\gtrsim1000$ for C^{5+}) hardly contribute to the value of P_{FR} at all [27]. For typical TSR parameters recombined C^{5+} ions are ionized for $n'\gtrsim60$ by demerging and for $n'>n_R\approx30$ by the subsequent bending magnet. Taking into account radiative stabilization to final states $n'\leqslant n_R=30$, we find a probability of $P_{\mathrm{FR}}\approx2.76\times10^{-10}$ for the ensemble investigated in Fig. 11 and Table I. By comparison, the probability for radiative recombination $P_{\mathrm{RR}}=n_e\alpha_{\mathrm{RR}}\tau_f$ amounts to 1.45×10^{-10} with $n_e=7\times10^6$ cm^{-3} and a standard rate coefficient [Eq. (2)] of $\alpha_{\mathrm{RR}}=3.45\times10^{-10}$ cm^3/s. Accordingly, the field-induced formation of Rydberg states during the merging followed by radiative stabilization is of the same order of magnitude as the standard RR process. The key point is that despite the low probability for forming bound states and the slow decay rate to lower n, the recombination rate α_{FR} will nevertheless be competitive with the similarly improbable process of radiative recombination.

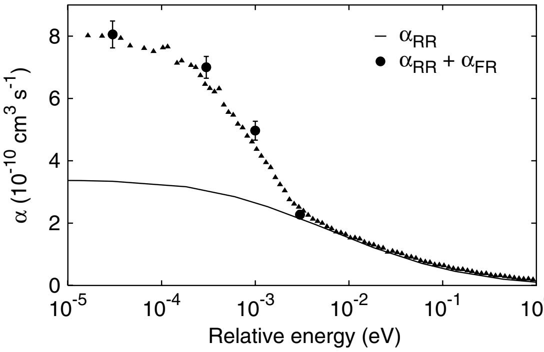

FIG. 15. Relative energy dependence of the recombination rate for C^{6+} ions at $B=42$ mT. The standard RR theory α_{RR} [Eq. (2)] (line), the experimental data [7] (▲), and the sum of the radiative stabilization [Eq. (23)] and standard RR rate, $\alpha_{\mathrm{FR}}+\alpha_{\mathrm{RR}}$, are displayed. $kT_{\parallel}=0.2$ meV, $kT_{\perp}=10$ meV, $n_R=30$, and $n_F=500$. The error bars refer to the statistical uncertainty in our simulation.

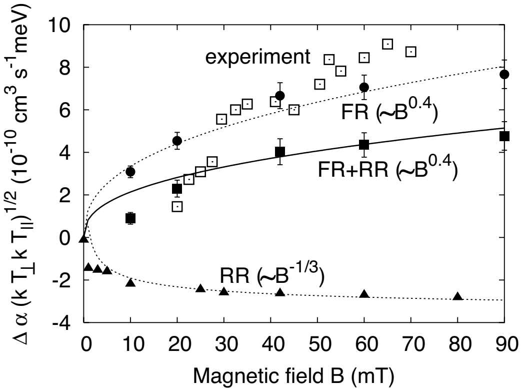

FIG. 16. Magnetic-field dependence of the excess recombination rate $\Delta\alpha$. Experimental data for C^{6+} [7] (□), α_{FR} with $n_F=500$ [Eq. (23)] (●, dashed line: $\propto B^{0.4}$), $\alpha_{\mathrm{RR}}^{B}-\alpha_{\mathrm{RR}}$ (▲, dashed line: $\propto B^{-1/3}$), and $\alpha_{\mathrm{FR}}+\alpha_{\mathrm{RR}}^{B}-\alpha_{\mathrm{RR}}$ (■, line: $\propto B^{0.4}$). $Z=6$, $kT_{\parallel}=0.2$ meV, $kT_{\perp}=10$ meV, and $n_R=30$.

V. COMPARISON WITH EXPERIMENT

We consider first only the effect of the magnetic field and compare α_{RR}^{B} and α_{RR} with the experimental data of Ref. [7] as a function of the average relative energy $\bar{E}$ between electrons and ions (Fig. 14). While the calculated rates agree with the experimental data and the standard RR theory for $\bar{E}\geqslant10$ meV, their behavior at smaller relative energies is quite remarkable. For $\bar{E}<kT_{\perp}$, α_{RR}^{B} displays a moderate enhancement while falling well below the Coulomb value α_{RR} for $\bar{E}\lesssim kT_{\parallel}$. The drop of α_{RR}^{B} below α_{RR} is consistent with the behavior of the visit function V_B at very small longitudinal velocities [Fig. 6(b)], where the Kepler motion in the pure ionic Coulomb potential brings an electron closer to the nucleus than the dynamics in the combined Coulomb and magnetic fields. The interplay between the suppression of visits at small $v_{\perp}$ and the enhancement of visits at higher $v_{\perp}$ determines the shape of the resulting recombination rates. As expected, for $B\rightarrow0$ the standard RR rate is recovered.

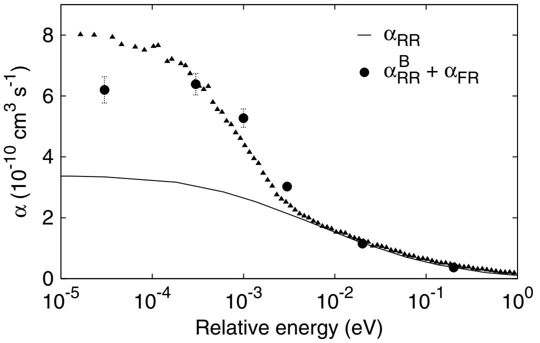

FIG. 17. Relative energy dependence of the recombination rate $\alpha^B_{\mathrm{RR}}+\alpha_{\mathrm{FR}}$ (●) in comparison with the standard rate (line) and experimental data (▲) (parameters as in Fig. 15).

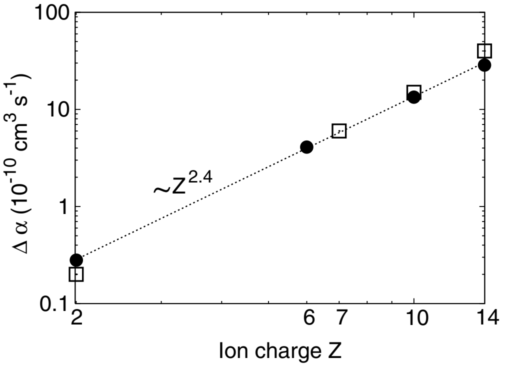

FIG. 18. Excess recombination rate $\Delta\alpha=\alpha_{\mathrm{tot}}-\alpha_{\mathrm{RR}}$ (●) as a function of the nuclear charge Z of the ion, □: CRYRING measurement (B=30 mT and $kT_\parallel$=0.12 meV) [6]. In the simulation n_R =10 (He^{2+}), 23 (C^{6+}), 35 (Ne^{10+}), and 43 (Si^{14+}). The dashed line is $\propto Z^{2.4}$.

Contributions only from the field-induced recombination followed by radiative stabilization increase the effective recombination significantly (Fig. 15) to values comparable to the experimental data. In the simulation of the radiative stabilization following field-induced recombination we have allowed small electric stray fields to be present ($\sim$2 V/cm) in the solenoid preventing states above $n_F\approx 500$ to be effectively stabilized as field ionization will immediately remove bound states with $n>n_F$. We have used n_R=30 (cutoff in the charge-analyzing dipole magnet) and τ_f=60 ns (total flight time through the solenoid delimited by the merging and demerging regions). Additional contributions due to the further decay of states with $30\lesssim n'\lesssim 60$ between the demerging region and the dipole magnet (additional time interval of $\sim$100 ns) to states with $n\lesssim 30$ are not included in the simulation, but are estimated to introduce errors of 20 percent into the present rate coefficients.

Figures 16–18 present results for the excess rates $\Delta\alpha$. Taking only the field-induced recombination into account, $\alpha_{\mathrm{FR}}-\alpha_{\mathrm{RR}}$, gives larger values than the total calculated excess rates. The reason is that the radiative recombination rate in the presence of the magnetic field α^B_{RR} falls significantly below the Coulomb value, i.e., $\alpha^B_{\mathrm{RR}}-\alpha_{\mathrm{RR}}$ is negative (see Fig. 16). The total excess rate is in reasonable agreement with the experimental data, both as a function of magnetic field (Fig. 16) and as a function of the relative energy (Fig. 17). Furthermore the scaling with the nuclear charge of the ion (Fig. 18) appears to reproduce experimental findings reasonably well.

We have also explored the perpendicular and parallel temperature dependence of $\Delta\alpha$ (Fig. 19). While the scaling of the excess recombination with $kT_\perp$ fitted by $(kT_\perp)^{-0.6}$ closely follows the experimental findings [7], we cannot reproduce the $(kT_\parallel)^{-0.5}$ behavior of the scaled excess rate $\Delta\alpha\sqrt{kT_\perp}$ observed in Ref. [7]. α_{FR} only weakly decreases with $kT_\parallel$ [$\alpha_{\mathrm{FR}}\sim(kT_\parallel)^{-0.03}$], but the total excess rate due to both RR and FR is seen slightly to increase as $(kT_\parallel)^{0.14}$ with the parallel electron temperature. Note that this rise in $\Delta\alpha$ originates from the behavior of α^B_{RR} at small relative velocities (compare Fig. 14). It should be noted that uncertainties in the determination of P_{FR} may arise from the extrapolation to low n values (compare Fig. 12), which limit the overall accuracy of the present simulation.

VI. CONCLUSION

We have studied two effects that alter the effective electron-ion recombination rate in a storage ring: the influence of the magnetic field in the solenoid and the effects of the transient electric field in the toroidal merging region. The magnetic field inside the solenoid of the electron cooler modifies the probability for radiative recombination of an electron with the target ion resulting in either enhancement or reduction. At zero relative energy, however, the magnetic field tends to suppress the recombination process. The enhancement of the recombination in cooler rings at very low relative energies originates primarily from transient field-induced recombination due to the merging of electron and

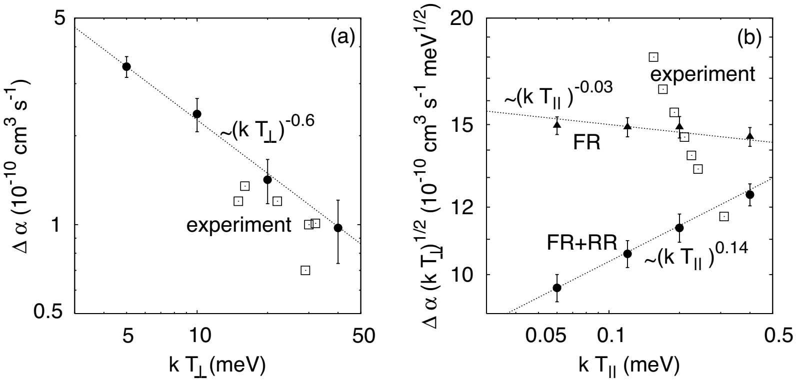

FIG. 19. Perpendicular (a) and parallel (b) temperature dependence of the calculated excess rate $\Delta\alpha$. $\alpha_{\mathrm{tot}}-\alpha_{\mathrm{RR}}$ (●), experimental data from the TSR experiment [7] (□) and in (b) α_{FR} (▲). In the CTMC B=42 mT, Z=6, n_R=30, n_F=500; $kT_\parallel$=0.2 meV (a) and $kT_\perp$=10 meV (b). The dashed lines are $\propto(kT_\perp)^{-0.6}$ (a), $(kT_\parallel)^{0.14}$ for the total excess rate, and $(kT_\parallel)^{-0.03}$ for FR alone (b). The rates in (b) are scaled with $\sqrt{kT_\perp}$ according to the perpendicular temperature dependence of the measurement.

ion beams, which, in combination with radiative stabilization inside the solenoid, presents a competitive route to recombination. We find absolute excess recombination rates in good agreement with the experimental data after the summation of the field-induced recombination rates and the radiative recombination rates in the magnetic field. The scaling of the excess rate with Z, B, $\bar{E}$, and $kT_\perp$ approximately agrees with the measurements, whereas the dependence on $kT_\parallel$ differs from the experimentally observed $(kT_\parallel)^{-1/2}$ scaling. The origin of this discrepancy is not yet known. We note that the enhancement of the recombination rate due to transiently formed bound states during the merging depends on the geometry of the merging and demerging sections. On the theoretical side, CTMC calculations with much larger ensemble sizes would be desirable, although at present computationally not feasible, in order to improve the representation of the calculated n distributions at low n values, thereby reducing the statistical uncertainties and extrapolation error of the recombination rate.

ACKNOWLEDGMENTS

We acknowledge support from the FWF P15025-N08 (Austria). G.G. acknowledges support from a University of Manitoba URGP.

---

[1] W. H. Tucker, *Radiation Processes in Astrophysics* (MIT University Press, Cambridge, 1975).
[2] H. P. Summers and W. J. Dickson, in *Application of Recombination*, NATO Advanced Studies Institute, Series B: Physics (Plenum, New York, 1992).
[3] M. Amoretti *et al.*, Nature (London) **419**, 456 (2002).
[4] G. Gabrielse *et al.*, Phys. Rev. Lett. **89**, 213401 (2002).
[5] H. Gao, D. R. DeWitt, R. Schuch, W. Zong, S. Asp, and M. Pajek, Phys. Rev. Lett. **75**, 4381 (1995).
[6] H. Gao, R. Schuch, W. Zong, E. Justiniano, D. R. DeWitt, H. Lebius, and W. Spies, J. Phys. B **30**, L499 (1997).
[7] G. Gwinner *et al.*, Phys. Rev. Lett. **84**, 4822 (2000).
[8] A. Hoffknecht *et al.*, Phys. Rev. A **63**, 012702 (2001).
[9] W. Shi *et al.*, Eur. Phys. J. D **15**, 145 (2001).
[10] A. Hoffknecht *et al.*, J. Phys. B **31**, 2415 (1998).
[11] O. Uwira *et al.*, Hyperfine Interact. **108**, 167 (1997).
[12] A. Hoffknecht, S. Schippers, A. Müller, G. Gwinner, D. Schwalm, and A. Wolf, Phys. Scr., T **92**, 402 (2001).
[13] A. Müller *et al.*, Phys. Scr., T **37**, 62 (1991).
[14] O. Uwira *et al.*, Hyperfine Interact. **108**, 149 (1997).
[15] M. Stobbe, Ann. Phys. (Leipzig) **7**, 661 (1930).
[16] H. A. Kramers, Philos. Mag. **46**, 836 (1923).
[17] H. A. Bethe and E. E. Salpeter, *Quantum Mechanics of One- and Two-Electron Atoms* (Plenum, New York, 1977).
[18] Q. Spreiter and C. Toepffer, J. Phys. B **33**, 2347 (2000).
[19] J. Hahn, J. Phys. B **34**, L701 (2001).
[20] M. Hörndl, S. Yoshida, K. Tökési, and J. Burgdörfer, in *Photonic, Electronic and Atomic Collisions*, edited by J. Burgdörfer, J. S. Cohen, S. Datz, and C. R. Vane (Rinton Press, Princeton, 2002), p. 324.
[21] M. Hörndl, S. Yoshida, K. Tökési, and J. Burgdörfer, Hyperfine Interact. **146/147**, 13 (2003).
[22] C. Heerlein, G. Zwicknagel, and C. Toepffer, Phys. Rev. Lett. **89**, 083202 (2002).
[23] M. Hörndl, S. Yoshida, K. Tökési, and J. Burgdörfer, Phys. Rev. Lett. **93**, 209301 (2004).
[24] C. Heerlein, G. Zwicknagel, and C. Toepffer, Phys. Rev. Lett. **93**, 209302 (2004).
[25] R. Abrines and I. C. Percival, Proc. Phys. Soc. Jpn. **88**, 861 (1966).
[26] C. O. Reinhold and C. A. Falcón, Phys. Rev. A **33**, 3859 (1986).
[27] M. Hörndl, S. Yoshida, A. Wolf, G. Gwinner, and J. Burgdörfer, Phys. Rev. Lett. **95**, 243201 (2005).
[28] E. Zerrad and Y. Hahn, J. Quant. Spectrosc. Radiat. Transf. **59**, 637 (1998).
[29] C. H. Iu, G. R. Welch, M. M. Kash, L. Hsu, and D. Kleppner, Phys. Rev. Lett. **63**, 1133 (1989).
[30] M. L. Du and J. B. Delos, Phys. Rev. Lett. **58**, 1731 (1987).
[31] J. B. Delos, S. K. Knudson, and D. W. Noid, Phys. Rev. Lett. **50**, 579 (1983).
[32] H. Friedrich and D. Wintgen, Phys. Rep. **183**, 37 (1989).
[33] L. D. Landau and E. M. Lifshitz, *Mechanics* (Pergamon Press, Oxford, 1960).
[34] S. G. Kuzmin, T. M. O'Neil, and M. E. Glinsky, Phys. Plasmas **11**, 2382 (2004).
[35] S. G. Kuzmin and T. M. O'Neil, Phys. Rev. Lett. **92**, 243401 (2004).
[36] M. Hörndl, S. Yoshida, K. Tökési, and J. Burgdörfer, Nucl. Instrum. Methods Phys. Res. B **235**, 290 (2005).
[37] C. Wesdorp, F. Robicheaux, and L. D. Noordam, Phys. Rev. Lett. **84**, 3799 (2000).
[38] C. Wesdorp, F. Robicheaux, and L. D. Noordam, Phys. Rev. Lett. **87**, 083001 (2001).
[39] G. Gwinner, D. Schwalm, and A. Wolf, in *XXII-ICPEAC, Abstracts of Contributed Papers*, edited by S. Datz, M. E. Bannister, H. F. Krause, L. H. Saddiq, D. R. Schultz, and C. R. Vane (Rinton Press, Princeton, 2001), p. 326.
[40] H. Marxer and L. Spruch, Phys. Rev. A **43**, 1268 (1991).
[41] M. W. Horbatsch, E. A. Hessels, and M. Horbatsch, Phys. Rev. A **72**, 033405 (2005).
[42] J. R. Guest and G. Raithel, Phys. Rev. A **68**, 052502 (2003).
[43] T. Topcu and F. Robicheaux, Phys. Rev. A **73**, 043405 (2006).